# Hydrogen abundance estimation and distribution on (101955) Bennu

A. Praet, M. A. Barucci, B. E. Clark, H. H. Kaplan, A. A. Simon, V. E. Hamilton, J. P. Emery, E. S. Howell, L. F. Lim, X. -D. Zou, et al.

# Hydrogen Abundance Estimation and Distribution on (101955) Bennu

Authors: A. Praet*[1], M. A. Barucci[1], B. E. Clark[2], H. H. Kaplan[3], A. A. Simon[3], V. E. Hamilton[4], J. P. Emery[5,6], E. S. Howell[7], L. F. Lim[3], X.-D. Zou[8], J.-Y. Li[8], D. C. Reuter[3], F. Merlin[1], J. D. P. Deshapriya[1], S. Fornasier[1,9], P. H. Hasselmann[1], G. Poggiali[10,11], S. Ferrone[2], J. R. Brucato[10], D. Takir[12], E. Cloutis[13], H. C. Connolly Jr[7,14], M. Fulchignoni[1], D. S. Lauretta[7].

[1]LESIA, Observatoire de Paris, Université PSL, CNRS, Université de Paris, Sorbonne Université, 5 place Jules Janssen, 92195 Meudon, France,
[2]Department of Physics, Ithaca College, Ithaca, NY, USA,
[3]NASA Goddard Space Flight Center, Greenbelt, MD, USA,
[4]Southwest Research Institute, Boulder, CO, USA,
[5]University of Tennessee, Knoxville, TN, USA,
[6]Northern Arizona University, Flagstaff, AZ, USA,
[7]Lunar and Planetary Laboratory, University of Arizona, Tucson, AZ, USA,
[8]Planetary Science Institute, Tucson, AZ, USA,
[9]Institut Universitaire de France (IUF), Paris, France,
[10]INAF–Arcetri Astrophysical Observatory, Florence, Italy,
[11]Department of Physics and Astronomy, University of Florence, Florence, Italy,
[12]JETS/ARES, NASA JSC, Houston, TX, USA,
[13]University of Winnipeg, Winnipeg, Manitoba, Canada R3B 2E9,
[14]Department of Geology, Rowan University, Glassboro, NJ, USA.

***Abstract:***
Asteroids were likely a major source of volatiles and water to early Earth. Quantifying the hydration of asteroids is necessary to constrain models of the formation and evolution of the Solar System and the origin of Life on Earth. The OSIRIS-REx (Origins, Spectral Interpretation, Resource Identification, and Security–Regolith Explorer) mission showed that near-Earth asteroid (101955) Bennu contains widespread, abundant hydrated phyllosilicates**, indicated by a ubiquitous absorption at ~2.7 µm. The objective of this work is to quantify the hydration—that is, the hydrogen content—of phyllosilicates on Bennu's surface and investigate how this hydration varies spatially. We** analyse spectral parameters (**normalized optical path length,** NOPL; **effective single-scattering albedo,** ESPAT; **and** Gaussian modeling) computed **from** the hydrated phyllosilicate absorption band of spatially resolved visible–near-infrared spectra acquired by OVIRS (the OSIRIS-REx Visible and InfraRed Spectrometer)**. We also computed the** same spectral parameters **using** laboratory-measured **spectra of meteorites including** CMs, CIs, and **the ungrouped C2** Tagish Lake. We estimate the mean hydrogen content of water and hydroxyl groups in hydrated phyllosilicates on Bennu's surface to be 0.71 ± 0.16 wt.%. This value is consistent with the hydration range of some aqueously altered meteorites (CMs, C2 Tagish Lake), but not the most aqueously altered group (CIs). The sample collection site of the OSIRIS-REx mission has slightly higher hydrogen content than average. Spatial variations in hydrogen content on Bennu's surface are linked to geomorphology, and may have been partially inherited from its parent body.

***Keywords:*** Asteroid Bennu; Asteroid Surfaces; Asteroid Composition; Meteorites; Spectroscopy.

* Corresponding author. alice.praet@obspm.fr (A. Praet).

## 1. Introduction

The OSIRIS-REx Visible and InfraRed Spectrometer (OVIRS) (Reuter et al., 2018) collected visible–near-infrared (VNIR) spectra in the range of 0.4 to 4.3 µm during the spacecraft's approach to and global mapping of Bennu (Lauretta et al., 2017). Early observations showed that Bennu's strongest spectral feature is the absorption band **in the 3-µm region** (at 2.74 ± 0.01 µm **for Bennu)** associated with the presence of $OH^-$ or $H_2O$ bound in hydrated phyllosilicates (Hamilton et al., 2019). The band position and ubiquity of **this feature on Bennu** indicates the global presence of Mg-phyllosilicate minerals that are the result of an advanced stage of hydrothermal alteration (Hamilton et al., 2019).
**In addition, Simon et al. (2020b) found minor absorption bands (characterized by a depth less than 5%) centered near 1.4, 1.8, and 2.3 µm, among others. The 1.4-µm absorption band is due to the first overtone of the OH stretch band (Clark et al., 1999), and the band near 1.8 could be associated with the combination the $H_2O$ bending and the OH stretch that occurs near 1.9 µm (Clark et al., 1999). As for the minor absorption band detected near 2.3 µm, it is insufficiently clear whether it is due to phyllosilicates (cation–OH bound), carbonates, or other species (Simon et al., 2020b).**
Bennu is **a** rubble-pile asteroid, **believed to be** part of the **Eulalia/New Polana families** that reaccumulated from the fragments of a ~100-km-diameter parent asteroid that was broken apart by impacts (Bottke et al., 2015; DellaGiustina and Emery et al., 2019; Jutzi and Michel, 2020; Michel and Ballouz et al., 2020; Walsh et al., 2013). **Through simulations, Michel and Ballouz et al. (2020) predicted that Bennu could originate from the catastrophic disruption of an already hydrated parent body sourced from a localized region, and that similarly heated unbound material during collision could result into a homogenous asteroid surface. This is consistent with Amsellem (2020) who, using radiometric dating of five heated CM carbonaceous chondrites, found that the CM heating event (at least 3 Ga after the Solar System formation) could have correlated with the parent-body disruption (i.e., the asteroid family-forming event) of New Polana and Eulalia families, for example, with age estimations of 1.4 ± 0.15 Ga and 0.8 ± 0.1 Ga, respectively (Walsh et al., 2013; Bottke et al., 2015).**
Image data acquired by OSIRIS-REx showed that Bennu has a rough and rocky surface covered with boulders up to ~100 m in longest dimension (Daly et al., 2020; DellaGiustina & Emery et al., 2019; Jawin et al., 2020; Walsh et al. 2019). There are two distinct populations of boulders distinguishable by their albedo, texture and thermal inertia (DellaGiustina et al., 2020). The low-reflectance population (≤4.9% normal albedo) has a rough, hummocky texture and encompasses a range of sizes. The high-reflectance population (>4.9% normal albedo) has smoother and more angular features and includes only boulders <~20 m. In the global map of the 2.7-µm hydration band depth (spectrum spot spatial resolution of ~20 m x 30 m per spectrum, map spatial resolution of ~600 $m^2$), the shallowest band depths are associated with the darkest boulders, which are also the hottest, as well as with the equatorial band (-20° to 20° latitude) (Simon et al., 2020**a**, see also **Figure 4**), which may be due to the differences in the mineralogy resulting from aqueous alteration (Kaplan et al., 2020).

The closest spectral analogs to Bennu (Clark et al., 2011) and other **low albedo** asteroids (e.g. Clark et al., 2010; Fornasier et al., 1999) are carbonaceous chondrite (CC) meteorites,

which have a continuum of mineralogical, petrological, and textural properties resulting from mild to strong aqueous alteration on their parent bodies. These properties can be used to constrain scenarios of geological evolution of small planetary bodies within the early solar system material (McSween et al., 2018). VNIR reflectance spectra of these meteorites measured in the laboratory have been analyzed to understand the spectral properties of hydrated minerals associated with varying degrees of alteration (Garenne et al. 2016; Potin et al. 2020; Takir and Emery, 2015). The first spectral behaviour analysis of the data from the OSIRIS-REx spacecraft, even if different from all available meteorites, showed that Bennu is most consistent with CM or CI chondrites (Hamilton et al., 2019), which are the most aqueously altered of the CC meteorites.

Previous studies of CM and CI chondrite hydration indicate that these meteorites have a range of hydration (defined as hydrogen wt.% in $H_2O$ and $OH^-$) that is correlated with the degree of alteration (**Robert and Epstein, 1982**; Alexander et al., 2007, 2012, 2013). These bulk-composition studies made assumptions about where hydrogen is hosted—for example, in minerals as opposed to organics—because direct detections of $H_2O$ and $OH^-$ *in situ* were not possible. However, subsequent studies found that most hydrated species are hosted in phyllosilicates, in particular Mg- and Fe-serpentines and saponite (Takir et al., 2013). Howard et al. (2015) showed that the majority of hydrogen is contained in phyllosilicates for the CM, ungrouped type 2, and CR chondrites. Phyllosilicate composition changes from Fe-rich to Mg-rich with increasing alteration (**McSween, 1979**).

Laboratory studies of C chondrites have shown how hydration may be quantified from VNIR spectra (**Pommerol and Schmitt, 2008a, 2008b and references therein**). Milliken and Mustard (2007) developed an approach where the effective single-particle absorption thickness (ESPAT) and the normalized optical path length (NOPL) of a spectrum can be linked directly to water content (see also Milliken and Mustard, 2005; Garenne et al., 2016). This approach has since been applied to global spectral datasets from Mars (e.g. Mustard et al., 2008) and the Moon (e.g. Li and Milliken, 2017). A similar study using H wt.% and spectra of C chondrites found that ESPAT and band depth can be used to estimate hydration for these meteorites (Garenne et al, 2016). Other analyses of C chondrites showed that Gaussian modeling of the 2.7-µm absorption feature could be directly related to H wt.% of the samples (Kaplan et al., 2019; Potin et al., 2020).

Correlation between meteorite spectral parameters and their hydration, defined as H content of the water and hydroxyl groups ($H_2O$ and $OH^-$) in the hydrated phyllosilicates (hereafter, H content) allowed us to estimate Bennu's surface H content, using Bennu spectral parameters. We discuss how Bennu H content estimation compares to the ones of CC meteorites. We, then, explore in detail how the hydration of Bennu's surface spatially varies. The implications of the H content estimation as well as its spatial variations are fundamental for the understanding of the cosmochemical history and aqueous alteration of Bennu's parent body, as well as for the sample of Bennu that the OSIRIS-REx spacecraft will return to Earth in 2023 (Lauretta et al., 2017).

## 2. Data and Methods

### 2.1 Bennu data

In April 2019, OVIRS, onboard the OSIRIS-REx spacecraft, acquired visible-infrared spectra, from 0.4 to 4.3 µm, of asteroid (101955) Bennu from a range of 5km. Global coverage was obtained at a solar phase angle of 8-10 degrees, with approximately 30% overlap from one spectrometer spot to the next (Simon et al., 2020**a**). **The** Bennu spectral data **we** used were acquired during the **third** Equatorial Station (EQ3) of the Detailed Survey phase, on May 9 2019, at 12:30 pm local solar time (Lauretta et al., 2017). This data set allows both careful spectral analysis at a spectral resolution of 2 nm from 0.4 to 2.4 µm and 5 nm **from 2.4 to 4.3 µm**, and global mapping at a spatial resolution of 20x30 meters per spectrum.
Spectra acquired were then calibrated and resampled. Finally, the thermal tail of each spectrum is removed and all spectra are divided by solar flux (Simon et al., 2020**a**) and then photometrically corrected (Zou et al., **2021**). The spectra were filtered according to their viewing geometry with incidence and emergence angles both inferior to 70°, to eliminate viewing geometry artefacts. Spectra were also filtered for spikes and saturation. Our data set after filtering is 7089 spectra for EQ3 station.
The OVIRS spectral reflectance of Bennu's surface depends on the light scattering geometry. In order to make comparisons between different areas and quantitatively interpret the spectra based on laboratory measurements, the observations need to be photometrically corrected to the same geometry. We choose a common geometry often used in laboratory settings, where Reflectance Factor (REFF) is measured at ($i_0$, $e_0$, $\alpha_0$) = (0°, 30°, 30°). OVIRS data are obtained in units of Radiance Factor (RADF). A McEwen model is used to correct the measured RADF values of each spectral wavelength to the reference geometry. Then, RADF data are converted to units of REFF for comparison with laboratory measurements. The details of the photometric correction are explained in (Zou et al., **2021**).

The OVIRS spectra are calibrated on a spot-by-spot basis using an automated pipeline that subtracts a nearby deep space background level, subtracts out-of-band signal (IR leakage in all filters < 2.95 µm), converts to absolute physical radiance units and screens for outlier pixels (Simon et al., 2018). Each spectrum is then resampled onto a common wavelength axis with 2-nm sampling below 2.4 µm and 5-nm sampling above 2.4 µm. As part of the signal above 2**.2** µm is from thermal radiance, a thermal tail is calculated and removed from each spectrum before dividing by a range-corrected solar spectrum to convert to reflectance (Simon et al., 2020**a**). There are two sources of uncertainty in the final spectra: channel-to-channel noise, which is calculated based on read noise and photon noise, and absolute radiance calibration. The absolute radiometric uncertainty affects the overall radiance across the full spectrum with no particular wavelength dependence. However, two terms do have a spectral dependence that may affect the hydration band. First, the out-of-band signal is calculated by summing the long wavelength radiance and multiplying by coefficients for each wavelength derived from perfect blackbody source data. Any spot that covers a mixed temperature scene may potentially have an error in this correction that increases with decreasing wavelength in each filter segment (i.e., it is larger at 1.7 µm than at 2.9 µm). The second uncertainty comes from the thermal tail correction that may remove too much, or not enough, radiance, if the thermal tail fit is **not well determined**. Both of these contribute a few percent of uncertainty to the absolute radiance. The uncertainty plotted in Figure 1a represents the standard error of the mean normalized spectrum.

## 2.2 Meteorite data

The meteorite dataset that we assembled for this study is composed of 39 hydrated CC meteorites (**Appendix A**) for which bulk hydrogen values have been independently measured (Alexander et al., 2012, 2013; Garenne et al., 2016).

All the selected meteorites used in this work, were powdered and spectra were measured under asteroid-like conditions (vacuum- and thermally-desiccated conditions) (**Appendix A**). Meteorite chips from Takir et al. (2013, 2019) were grounded into ~100-µm powder and no grain size distributions were measured due to the small amount of meteorite sample. The meteorites from Potin et al. (2020) and Garenne et al. (2016) were powdered manually but not sieved to keep a large grain size distribution.

An additional spectrum was collected for Mighei (with grain size < 500 µm) at INAF-Astrophysical Observatory of Arcetri in Firenze, Italy (*Poggiali personal communication*). Milliken and Mustard (2007) studied the effect of increasing spectrum particle size class (from <25 µm to 125–250 µm) on spectral parameters such as NOPL and ESPAT calculated on the spectrum 2.7-µm hydration band. They showed that these spectral parameters increase with increasing particle size for the same water content ($H_2O$ wt.%) of the sample. The meteorite spectra chosen in this study all present large grain size distribution with different maximum grain size. This difference is not believed to impact spectral measurements, as small-sized material dominates the spectral signature of planetary surfaces or meteorite powders characterized by a large particle size distribution.

The meteorite H contents used in this study are calculated in Alexander et al. (2012, 2013). The authors have measured the bulk carbon content as well as bulk hydrogen content. Assuming all carbon is in the organic matter, they then deduced the organic hydrogen content using the typical Insoluble Organic Matter (IOM) hydrogen to carbon ratio of CR meteorites and CM meteorites. The organic hydrogen content is subtracted from the bulk hydrogen content to derive the bulk hydrogen content in water and hydroxyl groups of hydrated phyllosilicates, i.e.: **H content** which is reported in **Appendix A**. In the case of meteorites for which the H content**s** were not calculated by Alexander et al. (2012, 2013), we did the same calculations as explained above, using the meteorite bulk composition measurements (bulk, H, bulk C and H/C values) from the literature. In the case of the Orgueil and Tagish Lake meteorites, several samples were analyzed and several **different** hydrogen content values were ultimately derived (Alexander et al., 2012; Gilmore et al., 2019), and our results reflect the variability in the reported values.

## 2.3 I/F spectrum conversion into single-scattering albedo (SSA) spectrum

In order to calculate the effective single-particle absorption thickness (ESPAT) parameter, we converted Bennu photometrically corrected I/F spectra into single-scattering albedo spectra using the five-parameter form of **a** Hapke model (Li et al., 2007a, 2007b, 2009) that **includes** a single-scattering albedo term (ω), a single-term Henyey-Greenstein (HG) function (p) with an asymmetry factor (g), a roughness parameter (θ) and finally a shadow hiding opposition effect term (SHOE) characterized by its width (h) and its height ($B_0$). The two latter parameters are fixed to 0.11 and 2.06, respectively, as derived from the disk-integrated phase function based on the OCAMS images obtained during the approach to the asteroid in December 2018.

The Hapke model is then run on **the** global-surface spectral data set in order to obtained the following global Hapke modeling parameters for the model best fit: ω, g, θ, geometric

albedo and bond albedo and goodness-of-fit indicators root-mean-square (RMS), relative root-mean-square (RRMS). The best fit **is** deduced from the smallest chi-square test ($\chi^2$) value when searching in parameter space (**from** Li et al., in **revision**). The same Hapke Isotropic Multiple Scattering Approximation (IMSA) model (Hapke, 1993, 2002) was then re-run on global-surface I/F spectral data set (EQ3) using the previously obtained global Hapke modeling parameters (**i.e. the global average Hapke model parameters from Li et al., in revision**), with the porosity term calculated using Helfenstein and Shepard (2011), leaving SSA as a free parameter at every channel.

In the case of meteorite spectra measured in **the** laboratory: we apply several simplifications **to** the Hapke model (Beck et al., 2010). The simplifications (Garenne et al., 2016; Milliken and Mustard, 2007) are the absence of opposition effects (no SHOE, no CBOE), therefore the backscattering term is negligible (B(g) = 0), and the phase function is **assumed to be** isotropic (the scattering term is set to p(g) = 1). These are reasonable **assumptions** for particulate samples in which particles are in **intimate** contact (powder) and larger in size than the wavelength (from 2.6 to 3.3 µm) (Milliken and Mustard, 2007).

### 2.4 ESPAT parameter calculation

The Effective Single Particle Absorption Thickness parameter ($W(\lambda)$, ESPAT) function is a quantity defined by Hapke (1993) related to the absorption coefficient, volume of particles and the single-scattering albedo (**Equation 1**).

Dealing with such quantities has proved to have some advantages: Hapke (1993) has shown that the ESPAT function is quasi-linear, proportional for a wide range of effective particle size determined by the value of internal scattered coefficient; subsequently, Milliken & Mustard (2005) found that this function is also linearly proportional for a wide range of absolute water content (0-15 %wt $H_2O$). ESPAT function is, therefore, most useful when the medium consists of particles that are sufficiently small (Hapke, 1993) or surface roughness equivalent to small particle size. It also indicates that the water content is quasi-linear in respect with the effective particle size.

When the extinction coefficient ($Q_E(\lambda)$) is assumed to be 1, then the scattering coefficient ($Q_S(\lambda)$) is equivalent to the volume-average single-scattering albedo ($\omega(\lambda)$). Thus, the ESPAT parameter can be calculated using volume-average single-scattering albedo ($\omega$) (**Equation 1**), Milliken and Mustard (2007).

$$W(\lambda) = \frac{1-\omega(\lambda)}{\omega(\lambda)} \qquad (\mathbf{1})$$

**Equation 1** shows that when there is no absorption ($\omega(\lambda) = 1$), the ESPAT parameter is null ($W(\lambda) = 0$). However, for dark material: $\omega(\lambda)$ values are **less than** 1 in **the** OVIRS wavelength range (0.4 to 4.3 µm), even when no absorption occurs. Therefore, following Milliken and Mustard (2007), we divide $\omega(\lambda)$ values by their continuum fits (using the maximum single scattering albedo value: $\omega_{max}(\lambda)$) to isolate the absorption band studied, with the following equation (**Equation 2**):

$$W(\lambda) = \frac{1-\frac{\omega(\lambda)}{\omega_{max}(\lambda)}}{\frac{\omega(\lambda)}{\omega_{max}(\lambda)}} \qquad (\mathbf{2})$$

**A** linear continuum is fitted using the reflectance average of three OVIRS wavelength channels as left and right anchor points (at 2.6 and 3.3 µm). The mean wavelength of the hydration band minimum position for the EQ3 data set corrected with McEwen model is

2.73 ± 0.01 µm; therefore, the ESPAT parameter was calculated at 2.73 µm, using also three-wavelength channel average.

### 2.5 NOPL parameter calculation

The normalized optical path length (NOPL) is calculated on absolute reflectance spectra of Bennu's surface and meteorites following the calculation of Milliken and Mustard (2007, see also Garenne et al., 2016; Milliken and Mustard, 2005; Milliken et al. 2007). The NOPL parameter at a defined wavelength (λ, here 2.73 µm) is calculated using the reflectance (R(λ)) as well as the reflectance of the linear continuum ($R_c(\lambda)$) fitted between 2.6 µm and 3.3 µm (**Equation 3**). We computed three-wavelength channel average for each linear continuum anchor point as well as for the centre point.

$$NOPL(\lambda) = \frac{-ln(R(\lambda)+1-R_c(\lambda))}{-ln(1-R_c(\lambda))} \qquad (3)$$

### 2.6 Band gaussian modeling

#### 2.6.1 3-µm Region Absorption Band

**The absorption band in the 2.7-µm region is caused by the combination of vibration fundamental mode and overtones of $H_2O$, OH, and cation–OH bonds.**

**$H_2O$ and OH groups are present in the mineral structure of phyllosilicates or can be adsorbed onto the surface of mineral grains in the case of $H_2O$. In the scope of this work, we focus our analysis on the absorption contribution of OH and $H_2O$ in the region between 2.6 and 3.3 µm.**

**The hydroxyl O—H bond has one stretching vibration fundamental mode, which depends on the cation to which the OH is bonded (Bishop et al., 2002). It can occur between 2.67 (Farmer, 1974) and 3.45 µm (Ryskin, 1974), and more typically between 2.7 and 2.8 µm (Clark et al., 1990). Absorptions near 2.72 and 2.75–2.76 µm are characteristic to magnesium-rich (Mg-OH) and aluminium-rich (Al-OH) phyllosilicates, respectively (DeSanctis et al., 2016). The OH stretch vibration of iron-rich (Fe-OH) phyllosilicates occurs near 2.8 µm (Manceau et al., 2000). Water ($H_2O$) in minerals is characterised by three vibration fundamental modes ($\nu$). A symmetric OH stretch in the water molecule ($\nu_1$) occurs near 3.106 µm and the asymmetric OH stretch ($\nu_3$) occurs near 2.903 µm, whereas the H-O-H bend ($\nu_2$) occurs near 6.079 µm (Clark et al., 1990). Adsorbed water was also found to cause an absorption band near 2.85 µm.**

#### 2.6.2 Gaussian modeling

**Gaussian modeling allows us to distinguish and define the different contributions of radical-OH and $H_2O$ stretching modes in the 2.7-µm region absorption band.**

The absorption band due to hydrated phyllosilicates in Bennu's spectra as well as in meteorite spectra were modelled using several Gaussians. The 2.7-µm region absorption band was modelled using Gaussians from 2.6 to 3.3 µm for Bennu's EQ3 average spectrum and using continuum anchor points adapted for each meteorite, using up to five Gaussian curve fits and a linear continuum.

Each Gaussian is diagnostic of one or several different stretching modes of $OH^-$ and/or $H_2O$ groups, depending on their center wavelength (2.72, 2.75, 2.8, 2.9 and 3.1 µm).

While these five Gaussian curves combine to create the composite absorption feature from ~2.6 to ~3.3 µm, each individual Gaussian curve is associated with energy required by a

slightly different hydrogen-rich functional group linked to hydroxyl ($OH^-$) and water ($H_2O$) (Clark et al., 1999; DeSanctis et al., 2017; Rivkin et al., 2015).

In our analysis, we use the area of the second Gaussian curve centered (on average) at 2.75 µm (hereafter the G2 area) that is associated with $OH^-$ (Kaplan et al., 2019). Of the three methods we have employed to assess H content of Bennu, Gaussian modeling of the absorption band has the highest number of free parameters and, as a result, the greatest uncertainty due to the large number **of** local **model** solutions, which leads to noisier results. We therefore have decided not to include Gaussian modelling results in our final **map of Bennu mean** H content, as we cannot distinguish spatial features within the noise. However, the gaussian modeling of the hydrated phyllosilicates is an independent test **to confirm the global average H content values obtained** from ESPAT and NOPL.

### 2.7 Mapping

In this study, we use the 200,000-facet Palmer shape model version 20 (Barnouin et al., 2019). For each facet, a weighted average value of the spectral parameter of all overlapping OVIRS spots is calculated using the percentage of overlap between OVIRS spot and the facet as weight **(Ferrone et al., 2021).** As described before, each spectrum thermal tail is removed and all spectra are photometrically corrected. **Finally,** all spectral parameter maps are overlaid on the global basemap (Bennett et al., 2020).

## 3. Results

We calculated the NOPL and the ESPAT parameters and performed Gaussian modeling of the 2.7-µm absorption band **for** the absolute reflectance spectra of a set of 39 meteorites (**Appendix A**). We find a linear correlation between **our** calculated spectral parameters and **the** H content of **the** meteorites. **Using this correlation**, we estimated the H content of Bennu's surface as well as its spatial variation, using the same spectral parameters calculated **from** Bennu's reflectance spectra.

### 3.1 Hydration Estimation

The spatially resolved spectral dataset of Bennu's global surface includes 7089 spectra, with incidence and emergence angles less than 70°, and covers Bennu's surface **from** –80°S and +80°N latitude. The average EQ3 Bennu spectrum is shown in **Figure 1a**. **Our** Gaussian model of Bennu's EQ3 average spectrum can be found in **Figure 1b**.

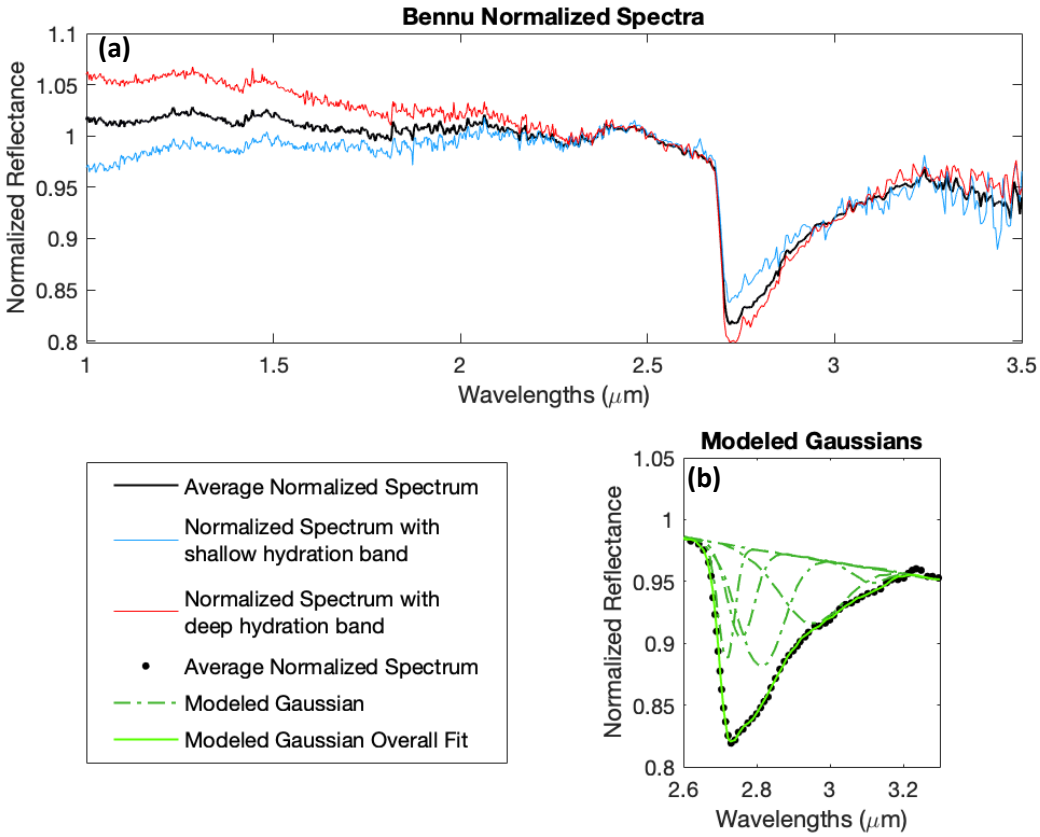


**Figure 1: a)** Average normalized **(at 2.5µm)** EQ3 Bennu spectrum with standard error of the mean (~$5.10^{-4}$), **as well as the spectra showing the deepest and shallowest hydration band in red and blue respectively**. **b)** Gaussian model result obtained for the average EQ3 spectrum (normalized to 1.0 @ 2.5µm), showing five separate Gaussian curves (dotted green lines), for which the composite spectrum (solid green curve), agrees well with the measured spectrum (blue dots).

We find a linear correlation between each of the spectral parameters (ESPAT, NOPL and Gaussian), **we** calculated from the meteorite spectra and the H content of the meteorites (**Figure 2, a to c**). The Spearman rank correlation was computed for each linear regression: the rank correlation coefficient ($R$) and the two-sided significance of its deviation from 0 ($p$-value) (**Figure 2**). In all three cases, the correlation is strong ($p$-value < 0.01 and $|R| > 0.6$).

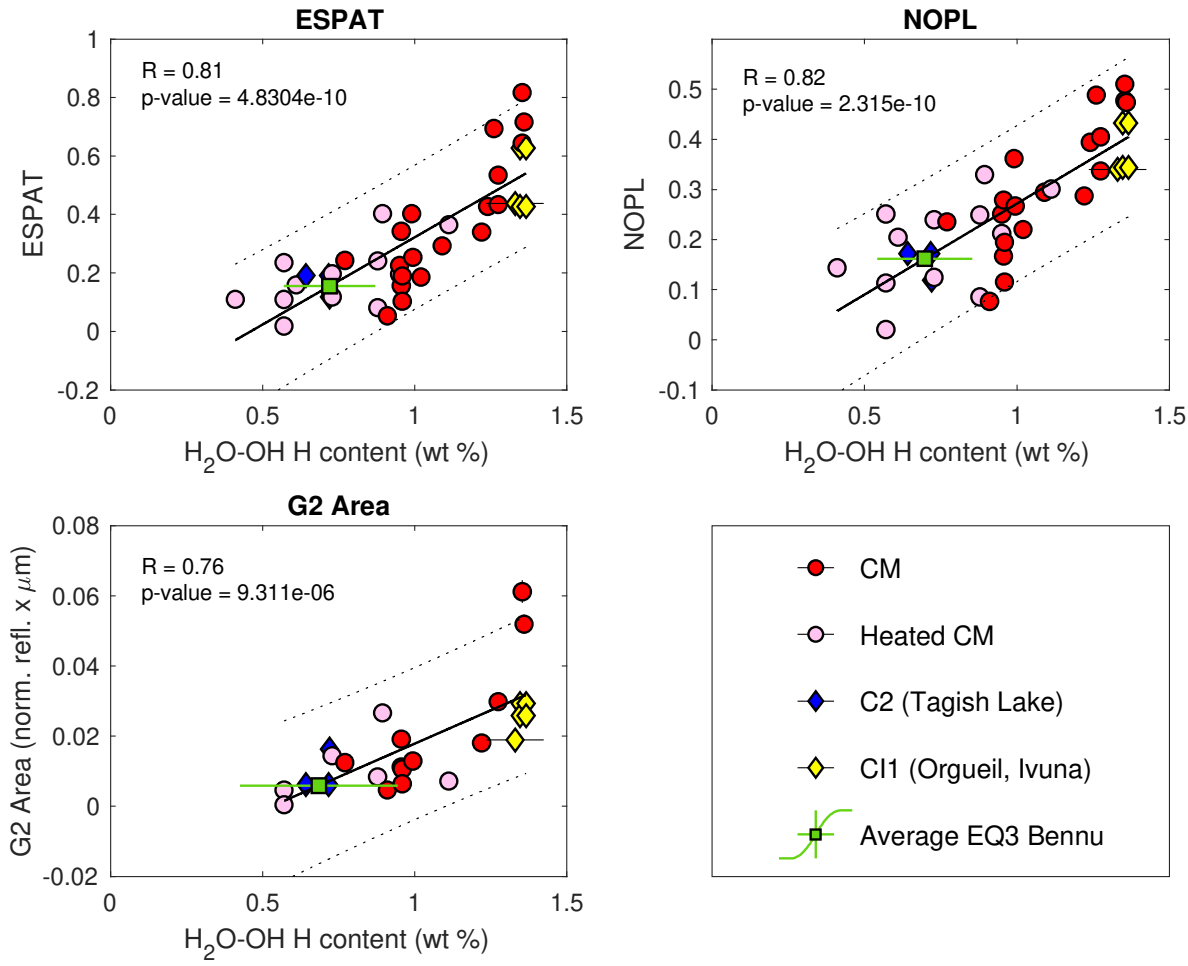


**Figure 2**: Linear correlation between the H content of meteorites (**Appendix A**) and **a)** their ESPAT parameter, **b)** the NOPL parameter, and **c)** G2 area, for different types of hydrated CC meteorites and Bennu. The thick black line is the linear regression of the meteorite data ; the two dashed black lines define the prediction bounds, which indicate the area in which a new data point would fall with 95% probability. Spearman rank correlation coefficient (*R*) and *p*-value are reported. Parameter errors for the meteorites are smaller than the symbols. The values for Bennu (**Table 1**) were determined by using the meteorite correlations. The vertical error bars on Bennu mean ESPAT, NOPL and G2 area are **their averaged uncertainty (Table 1) and are inside their symbol**. The H content horizontal bar is computed for each method by propagating the error in the determination of the linear regression coefficients **(which represents the uncertainty linked to the linear regression equation) as well as the mean uncertainty.**

We can therefore use the linear correlations between each spectral parameter and H content in the meteorites to estimate the H content of Bennu. **Figure 2** shows the average, maximum, and minimum values of each spectral parameter obtained from the EQ3 spectra of Bennu. The H content error is estimated using the propagation error associated **with** the linear correlation from the meteorites. We estimate the average H content of Bennu's surface to be 0.72 ± 0.15 wt.% using ESPAT, 0.70 ± 0.16 wt.% using NOPL, and 0.69 ± 0.26 wt.% using the G2 area. All average H content values that we derived for Bennu's surface are summarized in **Table 1**. The three different spectral parameters indicate consistent H content within the error bars. However, the Gaussian modeling method for G2 area presents

a large number of free parameters, and the non-**uniqueness** of **the Gaussian models** enhance its noise levels; therefore, we do not use the H content range derived from G2 area to compute **or map** the **mean** H content value of Bennu's surface. On the basis of the ESPAT and NOPL methods**,** Bennu's surface mean H content is 0.71 ± 0.16 wt.%. This range of values is consistent with the C2 Tagish Lake and heated CM meteorites and not consistent with the most heavily aqueously altered meteorites, the CIs (higher H content 1.330-1.366 wt.%, **Figure 2**). H content values obtained by measuring the NOPL parameter are consistent with values from ESPAT and G2 area fits to Bennu's 2.7-μm absorption band, which adds confidence to the result.

**Table 1:** Estimation of the **global** average H content **(phyllosilicate $H_2O$ and OH group hydrogen content)** of Bennu's surface derived from ESPAT, NOPL, and G2 area, **with the error derived from the uncertainties of each set of linear correlation coefficients.** The average H content computed with NOPL and ESPAT **methods** is also reported. **The mean value of each parameter as well as their associated mean uncertainty is reported in the first column.**

| **Parameter (Mean value ± uncertainty unit)** | **Estimated Bennu global average H content (wt.%)** |
|---|---|
| ESPAT (0.155 ± 0.010) | 0.72 ± 0.15 |
| NOPL (0.162 ± 0.010) | 0.70 ± 0.16 |
| G2 Area (0.006 ± 0.0007 normalized REFF.μm) | 0.69 ± 0.26 |
| NOPL & ESPAT avg | 0.71 ± 0.16 |

### 3.2 Hydration Variations

Maps showing the spatial variation of the NOPL and ESPAT parameters are shown in **Figure 3a** and **3b**, overlain on the global basemap of Bennu constructed from PolyCam images (Bennett et al., 2020). Both maps show a global pattern that is very similar to the hydration band depth map (Simon et al., 2020**a**) that we independently computed (**Figure 4**). Variations in the calculated spectral parameters are associated with albedo (DellaGiustina and Emery et al., 2019; Simon et al., 2020**a**) and morphological features on Bennu's surface. We find that Bennu's boulder-rich areas (Walsh et al., 2019) are characterized by lower NOPL and lower ESPAT. The equatorial band (–20° to 20° latitude) also shows lower NOPL and lower ESPAT. On the other hand, higher latitudes (low to intermediate boulder abundances) show higher values of NOPL and ESPAT (**Figure 3a** and **3b**). The ESPAT and NOPL maps show similar behaviour to the band depth (**Figure 4**), surface temperature, and albedo (Simon et al., 2020**a**). Simon et al. (2020**a**) report that the causes of the correlation between band depth and surface temperature are not **clear**, as **they could be due to** thermal tail removal method **or they could** be a function of surface properties (e.g., grain size effect, boulder thermal inertial, albedo, weathering, and composition) varying together.

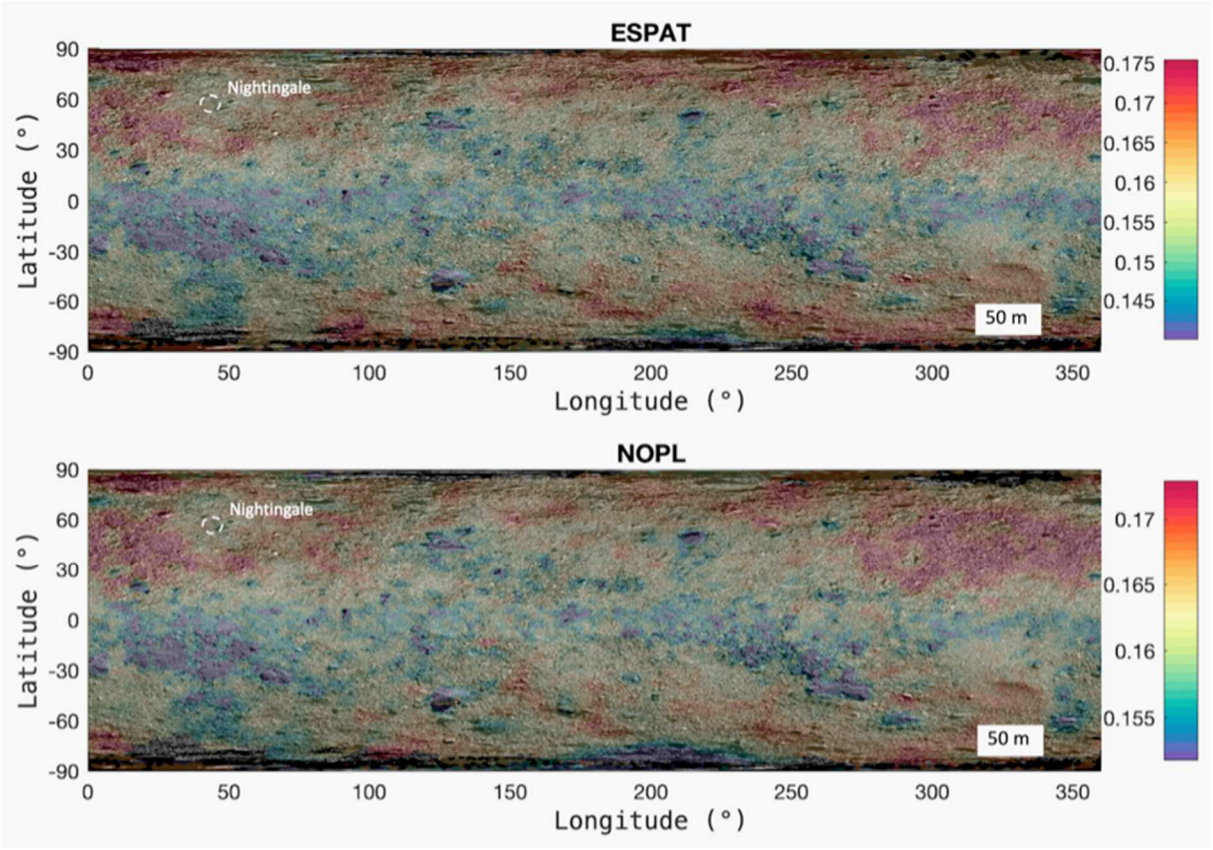


**Figure 3**: The ESPAT **(top)** and NOPL **(bottom)** parameters calculated for EQ3 spectra are respectively mapped on the global basemap of Bennu (Bennett et al., 2020). The OSIRIS-REx mission's **final selected site for sampling (Nightingale) is indicated.**

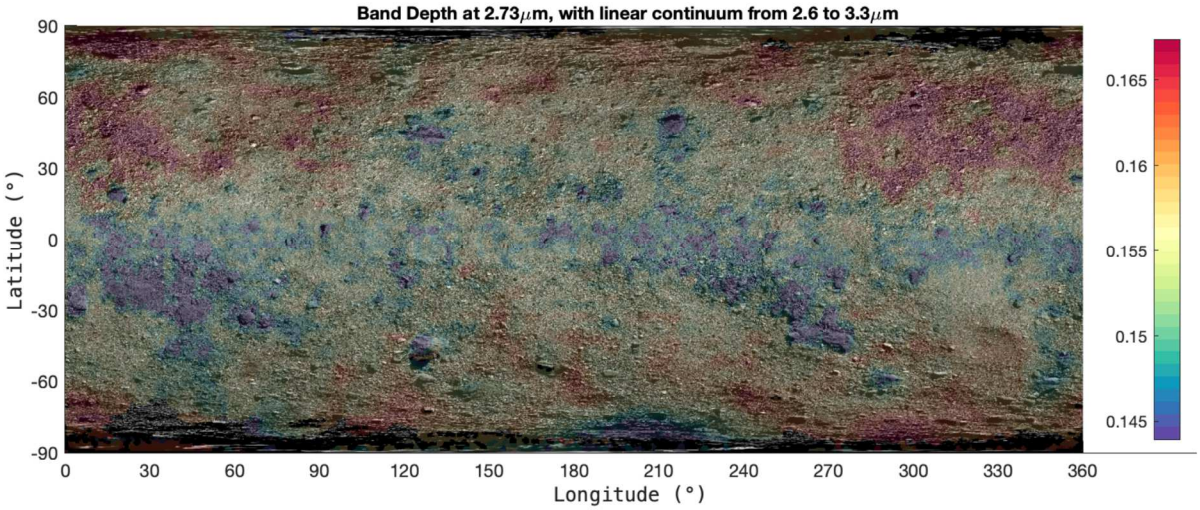


**Figure 4**: Band depth calculated at 2.73 µm, using a linear continuum from 2.6 to 3.3 µm, on EQ3 spectra (Simon et al., 2020a). **The uncertainties on the band depth are of the order of 1% (Simon et al., 2020a).**

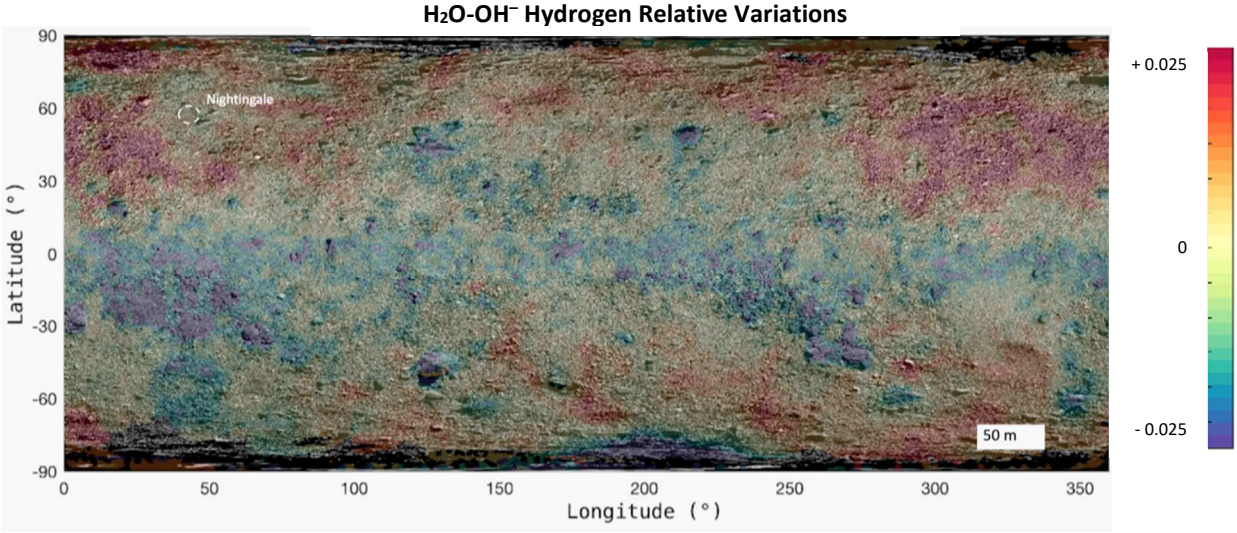


**Figure 5**: **The relative variation of the** average H content **(phyllosilicate $H_2O$ and OH group hydrogen content)** map of Bennu is derived from the average of the NOPL and ESPAT methods and overlain on the global basemap of Bennu (Bennett et al., 2020). **The zero value on the scale corresponds to the global average H content and the scale represent the H content variation with respect that zero value. The error of variation in H content is estimated with the error of the band depth measurement, which is of the order of 1%. The H content variation is in good agreement with the band depth variation (Figure 4).** The OSIRIS-REx mission's **final selected site for sampling (Nightingale) is indicated.**

The spatial variations of the average H content **(phyllosilicate $H_2O$ and OH group hydrogen content)** are overlain on the global basemap (Bennett et al., 2020) in **Figure 5**. **The relative variation of the average H content is in agreement with the band depth variation (Figure 4).** Lower H content is evident in boulder-rich areas (such as from 225 to 275 degrees longitude and 0 to –60° latitude). We observe several areas—including the boulders Benben Saxum (~56 m in diameter) and Roc Saxum (~95 m), and the Tlanuwa Regio, a region with a high density of large boulders (~50 m)—that are characterized by relatively low NOPL, low ESPAT, low H content (~0.66 wt.%), and shallow 2.7-µm band depths (Simon et al., 2020**a**).

In the equatorial band (–20° to 20° latitude), the H content is lower than average. This equatorial region is characterized by rubble-filled craters and a few boulders. Other workers have shown that the equatorial band has a higher thermal inertia than global average (Rozitis et al., 2020**a**), a stronger red spectral slope than global average (Barucci et al., 2020; Clark et al., 2019; **Fornasier et al., 2020**; Simon et al., 2020**a**), and a shallower hydration band depth (Simon et al., 2020**a**). The causes of these differences in the equatorial region may include space weathering, surface roughness variations due to mass movement (Barucci et al., 2020; Jawin et al., 2020), and/or preferential fall-back of particles ejected from Bennu's surface (McMahon et al. 2020).

We also find areas at intermediate to high latitudes (beyond 20° and –30°) that display deeper than average 2.7-µm band depths and higher than average ESPAT and NOPL values. These areas show the most hydration, with a higher than average H content of ~0.74 wt. % (see **Figure 5**, particularly at longitudes 0–100° and 275–360°). There are intermediate-size

boulders in these regions, and the surface has a higher than average albedo at 0.55 µm and lower abundances of the organic carbon surface components (Simon et al., 2020**a**). The **site from which the OSIRIS-REx spacecraft collected a sample**, Nightingale (56.0° N and 42.1° E), lies within this region, suggesting that the spacecraft is very likely to return a sample with relatively high H content in comparison to average Bennu, yet not as high as CIs.

## 4. Discussion

### 4.1 Spatial distribution of hydrogen

The patterns of high and low hydration on Bennu's surface likely reflect early processes on Bennu's parent body, as well as on-going modification of Bennu by space weathering, heating, and the drivers (meteoroid impacts, thermal fracturing, and/or dehydration of phyllosilicates) of the particle ejection events observed by the OSIRIS-REx mission (Hergenrother et al., 2020; Lauretta and Hergenrother et al., 2019). Some of these processes reduce hydration (e.g., impact-induced heating can cause dehydration, Nakamura, 2006), and others may increase the H+ ions on the surface (e.g., solar wind implantation, Li and Milliken, 2017; Tucker et al., 2019). Solar wind implantation of hydrogen has been shown to increase the 2.7-µm signature diurnally on the Moon, with higher hydrogen content at higher latitudes (Li and Milliken, 2017; **Clark, 2009; Pieters et al., 2009; Sunshine et al., 2009**). A similar spatial pattern of higher hydration at the poles is seen on Bennu, though it has not been noted on Ryugu (Kitazato et al., 2019). There is a strong relationship between observed hydration and temperature (Simon et al., 2020**a**), which is also the case for the implanted hydrogen on the Moon (Li and Milliken, 2017). Solar wind implantation is a surface process, meaning that our findings may not be representative of unexposed material on Bennu. **The lunar surface spectral data, acquired in 2017 by OVIRS, showed the 2.8 µm absorption band (Simon et al., 2019), which is consistent with the previous full-disk observations.**

Further, meteoroid bombardment would preferentially affect the equatorial region (Bottke et al., 2020) and could trigger a dehydration reaction; larger impacts in the equatorial region (as evidenced by the presence of large craters) could also have dehydrated material in the past. Boulders exposed for longer periods of time may also be more likely to experience similar dehydration processes. **Moreover, Jawin et al. (2020), analysing Bennu's surface morphology, concluded that mass movement appears to dominantly move from the mid-latitudes toward the equator, consequently altering the surface.**

Dehydration from impacts and implantation of $H^+$ by solar wind may together explain the **small** spatial variation in estimated H content **at the spatial resolution of the studied spectra of Bennu (20 × 30 m)**. **According to the modeling of Starukhina (2001), solar wind proton implantation may result in the creation of bands, but this is not confirmed in the spectroscopic survey of asteroids (Rivkin et al., 2003, 2015). Brunetto et al. (2020) showed that there is likely a solar wind contribution in the OTES data of Bennu's surface when they compared them with laboratory-irradiated meteorite spectra in the far infrared. Thus, we can expect a contribution from the solar wind proton implantation in the 2.7-µm region. However, spectral effects of space weathering are highly dependent on the initial physical and compositional properties of the material as shown by Lantz et al. (2018). Lantz et al. (2017) studied spectral effects associated with solar wind space weathering on carbonaceous chondrites and showed the 2.7-µm absorption band minimum position shifts to longer wavelength. Moreover, from spectral analysis of higher spatial resolution**

**OVIRS data of 45 craters on Bennu (Deshapriya et al., 2021), the 2.7-µm absorption band minimum position was found to have shifted to shorter wavelength for 20 craters with respect to the global average band minimum position, which has been attributed to the presence of less space-weathered (fresher) material in those craters. At the spatial resolution of the OVIRS spectral data set used in this study, the 2.7-µm band minimum position does not vary. Thus, with this analyzed spectral data set and because of the lack of supporting laboratory data, we cannot yet isolate the likely contribution of solar wind hydrogen implantation on Bennu's surface.**

Another consideration is differences in hydration originally inherited from the parent body of Bennu**.** The two main boulder types on Bennu**, which are well-mixed at all observed spatial scales,** may have had different initial compositions (e.g., resulting from spatially varying alteration) (Kaplan et al., 2020) and subsequent different reactions to space weathering (DellaGiustina et al., 2020). We find that regions with higher 0.55-µm reflectance on Bennu (**Figure 3D in** Simon et al., 2020**a**) generally have more hydrogen**, though variations are small** (**Figure 5**). In addition, the largest boulders on Bennu are dark (≤4.9% albedo; DellaGiustina et al., 2020) and are associated with lower hydration, as well as shallower band depth (Simon et al., 2020**a**), which suggests that some of the hydration signature is inherent to the discrete boulder population and likely reflects a dichotomy on Bennu's parent asteroid. From our dataset, we cannot separate the effects of space weathering, impact dehydration, or original composition.

### 4.2 Hydrogen abundance and comparison to meteorites

Bennu has similar H content (0.71 ± 0.16 wt.%) to the ranges found in CM meteorites (0.46–1.36 wt%), the ungrouped C2 meteorite Tagish Lake (0.50–0.69 wt.%), and CR meteorites (0.30–1.20 wt.%, Alexander et al., 2012). However, previous spectral analyses ruled out the CRs as analogs for Bennu and suggested that Bennu is most similar to the most aqueously altered CM and CI chondrites (Hamilton et al., 2019). However the H content of Bennu is not similar to those of the CIs (1.330–1.366 wt.%, Alexander et al., 2012, **Figure 2**).

Our results therefore indicate that Bennu is most similar to the CM and Tagish Lake meteorites. Most heated CMs have experienced temperatures of >~400°C (e.g. Lee et al., 2016). The estimation of H content, as shown here, and the fact that olivine has not been detected on the surface by OVIRS or OTES, both suggest that Bennu's phyllosilicates have not been significantly dehydrated or decomposed, which occurs at ~700°C (Hamilton et al., 2019; Hamilton et al., in **revision**). **The areas of lower H content on Bennu's surface correspond to higher surface temperature (~350 K) as shown in Figure 3C in Simon et al., 2020a. Moreover, Rozitis et al. (2020b), modelling Bennu's surface temperature, found modest seasonal temperature variations but relatively high diurnal temperature with a maximum of 390K at the equator during perihelion.**
The presence of organics in some locations on Bennu's surface could imply that these regions have not experienced significant heating (Kaplan et al., in prep; Kebukawa et al., 2010; Simon et al., 2020**a**), which could potentially rule out the heated CMs as analogs of Bennu, without excluding the lower end of heated CMs as evidence consistent with low to moderate heating are present on Bennu. Although Tagish Lake has a strongly red spectral slope (unlike the moderately blue slope of Bennu), it has previously been suggested to be

analogous to Bennu in terms of its carbonate-rich lithology, strong hydration feature, and low albedo (Kaplan et al., 2020; Merlin et al., **in revision**) as well as **by OTES comparison to laboratory spectral data (Brunetto et al., 2020).**

### 4.3 Hydrogen abundance and comparison with C-complex asteroids

**The relative abundance of phyllosilicates on asteroid surfaces has been the subject of studies of ground-based (Rivkin et al., 2003; Takir et al., 2019) and space-based observations (Ammannito et al., 2016; De Sanctis et al., 2016).**
**Ground-based observation campaigns of asteroids revealed the presence of 2.7-µm region absorption band in a number of asteroids (Rivkin et al., 2003; Rivkin et al., 2015, Takir & Emery, 2012). However, the 2.5–2.85 µm range remains difficult to analyse due to atmospheric absorption. The band minimum is generally situated in this wavelength range, limiting detailed mineralogical studies and comparison with carbonaceous chondrite.**

**The Dawn mission collected spatially resolved spectral data with near-global coverage of Ceres' and Vesta's surfaces using the visible and infrared mapping spectrometer (VIR) (De Sanctis et al., 2011) from 0.25 to 5µm. Ammannito et al. (2016) studied the repartition of phyllosilicates on the surface of Ceres using spectral data collected by VIR. The relative abundance of the Mg-bearing phyllosilicates was mapped using the intensity of its 2.72-to-2.73-µm centered absorption band and showed the variability of the Mg-bearing phyllosilicate abundance as well as a fairly uniform phyllosilicate composition across Ceres surface (with no significant variation of the band minimum position). Furthermore, using the VIR spectrometer in combination with the GRaND instrument (gamma ray and neutron detector) of the Dawn mission, Prettyman et al. (2019) analyzed the hydrogen elemental abundance at the surface of Ceres and Vesta. Prettyman et al., found that the majority of hydrogen is present in hydroxyl-bearing minerals at the surface of Vesta, while for Ceres, higher concentration of hydrogen in the poles is consistent with the presence of subsurface ice. However, the evolution histories and physical properties of these two objects are completely dissimilar from those of Bennu.**

**Spectroscopic surveys of C-complex and S-complex asteroids were performed using the Infrared Camera (from 2.5 to 5 µm) on board the satellite AKARI and the resulting asteroid spectral library was analyzed by Usui et al. (2019). They showed that the majority of observed C-complex asteroids present a significant 2.7-µm region absorption band, generally centered near 2.75 µm. They analyzed the relative abundance of hydrated phyllosilicates with a band depth calculation. Beck et al. (2020) discussed an approach to quantify the equivalent water abundance of main-belt asteroid surfaces using AKARI asteroid spectral data set in coordination with a set of laboratory measurements on carbonaceous chondrites under dry vacuum conditions (Beck et al., 2010). Using this newly available near-infrared spectral library of C-complex main-belt asteroids, Beck et al. (2020) computed a spectral metric and compared the results of those from laboratory-measured carbonaceous chondrite spectra as well as carbonaceous chondrite $H_2O$ abundances (wt.%) estimated by TGA (thermogravimetric analyses). The spectral metric they found, which can be applied to all meteorite types used in this study (CM, CI, CV, CR, CO, and Tagish Lake), uses the sum of the band depths at 2.75 and 2.8 µm. Through a linear correlation between**

**the previously mentioned spectral metric, they were able to estimate the water content at the surface of C-complex main-belt asteroids and determined a water content average of 4.5 wt.% $H_2O$ with high uncertainties of ± 4 wt.% $H_2O$ linked to the quality of the correlation. Beck et al. observed that the water content estimated for the most hydrated asteroids is lower than those of carbonaceous chondrites. This may be due to space weathering of asteroids or to an underestimation of the terrestrial water contribution in carbonaceous chondrites. While Bennu's spectra are of higher resolution and quality than AKARI's asteroid observations, the global H content estimation for Bennu gives only an indication of the surface hydration without disentangling the space weathering effects on Bennu's surface.**

## 5. Conclusions

These results represent the first spatially resolved estimation of hydrogen content in water and hydroxyl groups of hydrated phyllosilicates of an asteroid surface, revealing the presence of small latitudinal differences in H content as well as differences associated with geomorphology. Our results suggest that Bennu is moderately hydrated compared to CC meteorites, with an average H content of ~0.71 ± 0.16 wt.% derived from the NOPL and ESPAT methods. Long-term, on-going surface modification processes, including solar wind implantation and impact dehydration, may be responsible for the lower H content in the equatorial region. In addition, different initial compositions inherited from Bennu's parent body (DellaGiustina et al., 2020) may play a role in the distribution of H content, as exemplified by large, dark individual boulders with lower than average H content.

Quantifying the H content at the surface of Bennu **can constrain its thermal history and** help us to understand the composition of the primitive asteroid populations. The H content variations on Bennu, the full range of which is 0.64 ± 0.15 to 0.76 ± 0.15 wt.%, are small compared to the overall range of the CC meteorites used in this study (0.410 ± 0.001 to 1.366 ± 0.015 wt.%), which could validate the use of non–spatially resolved investigations of the 2.7-μm feature on asteroids to understand hydration and/or relation to the CC meteorites (e.g., with ground- or space-based telescopes). The study of $H_2O$ and $OH^-$ abundance on many primitive bodies can help constrain models of the formation and evolution of our Solar System, as well as some of the key processes in the development of life on Earth (Brack, 1993).

**The origin of water on Earth is one of the most important topics still debated (Alexander et al., 2012; Altwegg et al., 2015; Piani et al., 2020)**, i.e. how the Earth acquired so much water, having originated from a hot, dry part of the disk of gas and dust from which the Solar System formed. **Many primitive asteroids once contained abundant water, now stored as OH in hydrated minerals (Alexander et al. 2012). Therefore, the H content (phyllosilicate $H_2O$ and OH group hydrogen content) as well as its distribution found for Bennu's surface could help to constrain and model the compositional evolution of the pristine asteroid population.**

Two of the key ingredients for life, water and complex organic molecules, may have been delivered to Earth after formation by impacts with small bodies (Altwegg et al., 2019). OSIRIS-REx sampled Bennu's surface at site Nightingale in October 2020 and will return the collected sample to Earth in 2023; **the sample is predicted to contain** water and organics. **As Beck et al. (2021) estimated the water content for the most hydrated asteroids to be lower**

**than those of carbonaceous chondrites, we** suggest that the **hydrogen content contained in the phyllosilicate $H_2O$ and OH group** of the returned sample will be at least 0.71 wt.%. This hydrogen abundance is similar to those of the CM and Tagish Lake meteorites, which share similarities in phyllosilicate mineralogy with Bennu. **Our analysis does not allow to unravel the space weathering effects on Bennu's surface.**
Both the sample and the VNIR spectral data reflect the surface composition of Bennu, which may be more heated and/or space-weathered than material sourced from the interior. **Given that the OSIRIS-REx sample acquisition mechanism penetrated several centimetres into the subsurface (Lauretta et al., 2021),** weathered as well as potentially unweathered material will be returned. Our results, if validated by analysis of the returned sample, could be used to estimate H content on other hydrated asteroids.

**Acknowledgments**
We are grateful to the entire OSIRIS-REx Team for making the encounter with Bennu possible. This material is based upon work supported by NASA under Contract NNM10AA11C issued through the New Frontiers Program. French authors thank the French Space Agency CNES for financial support. PHH acknowledges funding support by DIM ACAV+ program by the region Ile de France. GP and JRB acknowledge support from the INAF – Astrophysical Observatory of Arcetri, which is supported by the Italian Space Agency agreement no 2017-37-H.0. This research uses spectra acquired at the NASA RELAB facility at Brown University. **We thank Catherine Wolner for editorial help. We thank the two anonymous referees for their comments and suggestions that helped improving this manuscript.**

**Data availability**
The OVIRS EQ3 spectral data used in this work are available via the Planetary Data System at https://sbn.psi.edu/pds/resource/orex/ovirs.html. Data are delivered to the PDS according to the OSIRIS-REx Data Management Plan available in the OSIRIS-REx PDS archive. **The maps are available upon request.** The meteorite data were obtained from the references shown in **Appendix A**.

**References**


- Alexander C.M.O'D., Fogel M.L., Yabuta H., Cody G.D., 2007. The origin and evolution of chondrites recorded in the elemental and isotopic compositions of their macromolecular organic matter. Geochim. Cosmochim. Acta 71(17), 4380-4403.

- Alexander C.M.O'D., Bowden R., Fogel M.L., Howard K.T., Herd C.D.K., Nittler L.R., 2012. The Provenances of Asteroids, and Their Contributions to the Volatile Inventories of the Terrestrial Planets**.** Science 337, 721-723.

- Alexander C.M.O'D., Howard K.T., Bowden R., Fogel M.L., 2013. The classification of CM and CR chondrites using bulk H, C and N abundances and isotopic compositions. Geochim. Cosmochim. Acta 123, 244-260.

- **Altwegg, K., et al., 2015. 67P/Churyumov-Gerasimenko, a Jupiter family comet with a high D/H ratio. Science 347.6220, doi: 10.1126/science.1261952**

- Altwegg, K., Balsiger, H., Fuselier, S. A., 2019. Cometary chemistry and the origin of icy solar system bodies: the view after Rosetta. Annual Rev. Astron. Astrophys. 57, 113-155.

- **Ammannito, E., et al., 2016. Distribution of phyllosilicates on the surface of Ceres. Science 353.6303, doi: 10.1126/science.aaf4279**

- **Amsellem, E., Moynier, F., Mahan, B., Beck, P., 2020. Timing of thermal metamorphism in CM chondrites: Implications for Ryugu and Bennu future sample return. Icarus, 339, 113593.**

- Barnouin, O.S., et al., 2019. Shape of (101955) Bennu indicative of a rubble pile with internal stiffness. Nat. Geosci. 12(4), 247-252.

- Barucci, M.A., et al., 2020. OSIRIS-REx spectral analysis of (101955) Bennu by multivariate Statistics, Astron. Astrophys. 637, L4.

- Beck, P., et al., 2010. Hydrous mineralogy of CM and CI chondrites from infrared spectroscopy and their relationship with low albedo asteroids. Geochim. Cosmochim. Acta 74(16), 4881-4892.

- **Beck, P., et al., 2020. "Water" abundance at the surface of C-complex main-belt asteroids. Icarus, 114125.**

- Bennett, C., et al., 2021. A High-Resolution Global Basemap of (101995) Bennu. Icarus 375, 113690.

- **Bishop, J., Murad, E., Dyar, M. D., 2002. The influence of octahedral and tetrahedral cation substitution on the structure of smectites and serpentines as observed through infrared spectroscopy. Clay Minerals, 37(4), 617-628.**

- Bottke, W.F., et al., 2015. In search of the source of asteroid (101955) Bennu: applications of the stochastic YORP model. Icarus 247, 191-217.

- Bottke, W.F., Moorhead, A., Connolly, H.C. Jr, 2020. Meteoroid Impacts as a Source of Bennu's Particle Ejection Events. J. Geophys. Res. – Planets, doi: 10.1029/2019JE006282.

- Brack, A., 1993. Liquid water and the origin of life. Origins of Life and Evolution of the Biosphere 23(1), 3-10.

- **Brunetto, R., et al., 2020. Characterizing irradiated surfaces using IR spectroscopy." Icarus 345, 113722.**

- **Clark, R. N., King, T. V. V., Klejwa, M., Swayze, G. A., Vergo, N., 1990. High spectral resolution reflectance spectroscopy of minerals, J. Geophys. Res., 95(B8), 12653–12680, doi:10.1029/JB095iB08p12653.**

- Clark, R.N., 1999. Spectroscopy of rocks and minerals, and principles of spectroscopy. Manual of remote sensing 3(3-58), 2-2.

- **Clark, R.N., 2009. Detection of adsorbed water and hydroxyl on the Moon. Science 326 (5952), 562-564, doi:10.1126/science.1178105.**

- Clark, B.E., et al., 2010. Spectroscopy of B-type asteroids: Subgroups and meteorite analogs. J. Geophys. Res. – Planets, 115(E6).

- Clark, B.E., et al., 2011. Asteroid (101955) 1999 RQ36: Spectroscopy from 0.4 to 2.5µm and Meteorite Analogs. Icarus 216, 462-475.

- Daly, M.G., et al., 2020. Hemispherical Differences in the Shape and Topography of Asteroid (101955) Bennu. Science Advances, doi: 10.1126/sciadv.abd3649.

- DellaGiustina, D.N., Emery, J.P., et al., 2019. Properties of rubble-pile asteroid (101955) Bennu from OSIRIS-REx imaging and thermal analysis. Nat. Astron., 3(4), 341-351.

- DellaGiustina, D.N., et al., 2020. Variations in Color and Reflectance of Asteroid (101955) Bennu. Science, doi: 10.1126/science.abc3660.

- **De Sanctis, M.C., et al., 2011. The VIR spectrometer. Space Science Reviews 163, 329-369.**

- **De Sanctis, M.C., et al., 2016. Bright carbonate deposits as evidence of aqueous alteration on (1) Ceres. Nature, 536(7614), 54-57.**

- De Sanctis, M.C., et al., 2017. Localized aliphatic organic material on the surface of Ceres. Science, 355(6326), 719-722.

- **Farmer, V.C., 1974. Infrared spectra of minerals. Mineralogical society.**

- **Ferrone, S., et al., 2021. Analysis of Projection Effects in OSIRIS-REx Spectral Mapping Methods: Recommended Protocols for Facet-Based Mapping. Earth Space Science, doi: 10.1029/2019EA000613**

- Fornasier, S., Lazzarin, M., Barbieri, C., Barucci, M.A., 1999. Spectroscopic comparison of aqueous altered asteroids with CM2 carbonaceous chondrite meteorites. Astron. Astrophys. Suppl. Ser., 135(1), 65-73.

- **Fornasier, S., et al., 2020. Phase reddening on asteroid Bennu from visible and near-infrared spectroscopy. Astron. Astrophys. 644, A142, https://doi.org/10.1051/0004-6361/202039552 .**

- Garenne, A., et al., 2016. Bidirectional reflectance spectroscopy of carbonaceous chondrites: Implications for water quantification and primary composition. Icarus 264, 172-183.

- Gilmour, C.M., Herd, C. D. K., Beck, P., 2019. Water abundance in the Tagish Lake meteorite from TGA and IR spectroscopy: Evaluation of aqueous alteration. Meteorit. Planet. Sci. 54, 1951–1972.

- Hamilton, V.E., et al., 2019. Evidence for widespread hydrated minerals on asteroid (101955) Bennu. Nat. Astron. 3(4), 332-340.

- **Hamilton, V. E. et al. (in revision). Evidence for limited compositional and particle size variation on asteroid (101955) Bennu from thermal infrared spectroscopy. *Astron. Astrophys.***

- Hapke, B., 1993. Theory of Reflectance and Emittance Spectroscopy. Cambridge University Press, Cambridge, UK.

- Hapke, B., 2002. Bidirectional reflectance spectroscopy: 5. The coherent backscatter opposition effect and anisotropic scattering. Icarus 157(2), 523-534.

- Helfenstein, P., Shepard, M.K., 2011. Testing the Hapke photometric model: Improved inversion and the porosity correction. Icarus 215(1), 83-100.

- Hergenrother, C.W., et al., 2020. Introduction to the Special Issue: Exploration of the Activity of Asteroid (101955) Bennu. J. Geophys. Res. – Planets, doi: 10.1029/2020JE006549.

- Howard, K.T., Alexander, C.M.O.'D., Schrader, D.L., Dyl, K.A., 2015. Classification of hydrous meteorites (CR, CM and C2 ungrouped) by phyllosilicate fraction: PSD-XRD modal mineralogy and planetesimal environments. Geochim. Cosmochim. Acta 149, 206-222.

- Jawin, E.R. et al., 2020. Global patterns of recent mass movement on asteroid (101955) Bennu. J. Geophys. Res. – Planets, doi: 10.1029/2020JE006475.

- Jutzi, M., Michel, P., 2020. Collisional heating and compaction of small bodies: constraints for their origin and evolution. Icarus, 113867.

- Kaplan, H.H., Milliken, R.E., Alexander, C.M.O.'D., Herd, C.D., 2019. Reflectance spectroscopy of insoluble organic matter (IOM) and carbonaceous meteorites. Meteorit. Planet. Sci. 54(5), 1051-1068.

- Kaplan, H.H., et al., in prep. Composition of Organics on Asteroid (101955) Bennu. Astron. Astrophys.

- Kaplan, H.H., et al., 2020. Bright carbonate veins on asteroid (101955) Bennu: Implications for aqueous alteration history. Science doi: 10.1126/science.abc3557.

- Kebukawa, Y., Nakashima, S. Zolensky, M.E., 2010. Kinetics of organic matter degradation in the Murchison meteorite for the evaluation of parent-body temperature history: Kinetics of organic matter degradation in the Murchison meteorite. Meteorit. Planet. Sci. 45, 99–113.

- Kitazato, K., et al., 2019. The surface composition of asteroid 162173 Ryugu from Hayabusa2 near-infrared spectroscopy. Science 364(6437), 272-275.

- **Lantz, C., et al., 2017. Ion irradiation of carbonaceous chondrites: A new view of space weathering on primitive asteroids. Icarus 285, 43-57.**

- **Lantz, C., Binzel, R.P., DeMeo, F.E., 2018. Space weathering trends on carbonaceous asteroids: A possible explanation for Bennu's blue slope? Icarus 302, 10-17.**

- Lauretta, D.S., et al., 2017. OSIRIS-REx: sample return from asteroid (101955) Bennu. Space Sci. Rev. 212(1-2), 925-984.

- Lauretta, D.S., Hergenrother, C.W. et al., 2019. Episodes of particle ejection from the surface of the active asteroid (101955) Bennu. Science, doi: 10.1126/science.aay3544.

- **Lauretta, D. S., et al., 2021. THE OSIRIS-REX TOUCH-AND-GO SAMPLE ACQUISITION EVENT AND IMPLICATIONS FOR THE NATURE OF THE RETURNED SAMPLE. 52nd Lunar and Planetary Science Conference.**

- Lee, M.R., Lindgren, P., King, A.J., Greenwood, R.C., Franchi, I.A., Sparkes, R., 2016. Elephant Moraine 96029, a very mildly aqueously altered and heated CM carbonaceous chondrite: Implications for the drivers of parent body processing. Geochim. Cosmochim. Acta 187, 237-259.

- Li, J.Y., et al., 2007a. Deep Impact photometry of comet 9P/Tempel 1. Icarus 187(1), 41-55.

- Li, J.Y., A'Hearn, M.F., McFadden, L.A., Belton, M.J., 2007b. Photometric analysis and disk-resolved thermal modeling of Comet 19P/Borrelly from Deep Space 1 data. Icarus 188(1), 195-211.

- Li, J.Y., A'Hearn, M.F., Farnham, T.L., McFadden, L.A., 2009. Photometric analysis of the nucleus of Comet 81P/Wild 2 from Stardust images. Icarus 204(1), 209-226.

- Li, J.Y., et al., **in revision**. Spectrophotometric modeling and mapping of (101955) Bennu and the implications. Planet. Sci. J.

- Li, S., Milliken, R.E., 2017. Water on the surface of the Moon as seen by the Moon Mineralogy Mapper: Distribution, abundance, and origins. Science Advances 3(9), e1701471.

- **Manceau A. et al., 2000. Oxidation-reduction mechanism of iron in dioctahedral smectites: II. Crystal chemistry of reduced Garfield nontronite. American Mineralogist, Volume 85, pages 153–172.**

- McMahon, J.W., et al., 2020. Dynamical Evolution of Simulated Particles Ejected from Asteroid Bennu. J. Geophys. Res. – Planets, e2019JE006229.

- **McSween Jr, H. Y., 1979. Alteration in CM carbonaceous chondrites inferred from modal and chemical variations in matrix. Geochimica et Cosmochimica Acta, 43(11), 1761-1770.**

- McSween, H.Y. Jr, et al., 2018. Carbonaceous chondrites as analogs for the composition and alteration of Ceres. Meteorit. Planet. Sci. 53(9), 1793-1804.

- Merlin, F., et al., **in revision.** In search of Bennu analogs: Hapke modeling of meteorite mixtures. Astron. Astrophys.

- Michel, P., Ballouz, R.-L., et al., 2020. Collisional formation of top-shaped asteroids and implications for the origins of Ryugu and Bennu. Nat. Comm., doi: 10.1038/s41467-020-16433-z.

- Milliken R.E., Mustard J.F., 2005. Quantifying absolute water content of minerals using near-infrared reflectance spectroscopy. J. Geophys. Res. 110, E12001, doi:10.1029/2005JE002534, 2005

- Milliken, R.E., Mustard, J.F., 2007. Estimating the water content of hydrated minerals using reflectance spectroscopy: II. Effects of particle size. Icarus, 189(2), 574-588.

- Milliken R.E., et al., 2007. Hydration state of the Martian surface as seen by Mars Express OMEGA: 2. $H_2O$ content of the surface. J. Geophys. Res. 112, E08S07, doi: 10.1029/2006JE002853

- Mustard, J.F., et al., 2008. Hydrated silicate minerals on Mars observed by the Mars Reconnaissance Orbiter CRISM instrument. Nature 454(7202), 305-309.

- Nakamura, T.Y., 2006. 793321 CM chondrite: Dehydrated regolith material of a hydrous asteroid. Earth Planet. Sci. Lett. 242, 26–38.

- **Piani, L., Marrocchi, Y., Rigaudier, T., Vacher, L.G., Thomassin, D., Marty, B., 2020. Earth's water may have been inherited from material similar to enstatite chondrite meteorites. Science, 369(6507), 1110-1113.**

- **Pieters, C.M., et al., 2009. Character and spatial distribution of OH/H2O on the surface of the Moon seen by M3 on Chandrayaan-1. Science, 326(5952), 568-572.**

- **Pommerol, A., Schmitt, B., 2008a. Strength of the H2O near-infrared absorption bands in hydrated minerals: Effects of measurement geometry. J. Geophys. Res. Planets, 113(E12).**

- **Pommerol, A., Schmitt, B., 2008b. Strength of the H2O near-infrared absorption bands in hydrated minerals: Effects of particle size and correlation with albedo. J. Geophys. Res. Planets, 113(E10).**

- Potin, S., Beck., P., Usui, F., Bonal, L., Vernazza, P., Schmitt, B., 2020. Style and intensity of hydration among C-complex asteroids: a comparison to desiccated carbonaceous chondrites. Icarus 348, 113826.

- **Prettyman, T.H., et al., 2019. Elemental composition and mineralogy of Vesta and Ceres: Distribution and origins of hydrogen-bearing species. Icarus 318, 42-55.**

- Reuter, D.C., et al., 2018. The OSIRIS-REx Visible and InfraRed Spectrometer (OVIRS): spectral maps of the asteroid Bennu. Space Sci. Rev. 214(2), 54.

- **Rivkin, A.S., et al., 2003. Hydrogen concentrations on C-class asteroids derived from remote sensing. Meteoritics & Planetary Science 38, Nr 9, 1383–1398.**

- Rivkin A.S., et al., 2015. Water and Hydroxyl on Asteroids. Asteroids IV (P. Michel et al., eds), 65-87. Univ. of Arizona Press, Tucson.

- **Robert, F., Epstein, S., 1982. The concentration and isotopic composition of hydrogen, carbon and nitrogen in carbonaceous meteorites. Geochim. Cosmochim. Acta 46, 81-95.**

- Rozitis, B., et al., 2020**a**. Asteroid (101955) Bennu's Weak Boulders and Thermally Anomalous Equator. Science Advances, doi: 10.1126/sciadv.abc3699.

- **Rozitis, B., et al., 2020b. Implications for ice stability and particle ejection from high-resolution temperature modeling of asteroid (101955) Bennu. J. Geophys. Res. Planets, 125, e2019JE006323. https://doi.org/10.1029/2019JE006323**

- Rubin, A.E., Trigo-Rodríguez, J.M., Huber, H., Wasson, J.T., 2007. Progressive aqueous alteration of CM carbonaceous chondrites. Geochim. Cosmochim. Acta 71, 2361-2382.

- **Ryskin, Y.I., 1974. The vibrations of protons in minerals: hydroxyl, water and ammonium. The infrared spectra of minerals, 137-182.**

- Simon, A.A., et al., 2018. In-Flight Calibration and Performance of the OSIRIS-REx Visible and IR Spectrometer (OVIRS). Remote Sensing, doi: 10.3390/rs10091486.

- **Simon, A.A., et al., 2019. OSIRIS-REx visible and near-infrared observations of the Moon. Geophysical Research Letters, 46, 6322–6326. https:// doi.org/10.1029/2019GL083341**.

- Simon, A.A., et al., 2020**a**. Widespread carbon-bearing materials on near-Earth asteroid (101955) Bennu. Science, doi: 10.1126/science.abc3522.

- **Simon, A.A., et al., 2020b. Weak spectral features on (101995) Bennu from the OSIRIS-REx Visible and InfraRed Spectrometer. Astron. Astrophys. 644, A148.**

- **Starukhina, L., 2001. Water detection on atmosphereless celestial bodies: Alternative explanations of the observations. J. Geophys. Res. Planets, 106(E7), 14701-14710.**

- **Sunshine, J.M., et al., 2009. Temporal and spatial variability of lunar hydration as observed by the Deep Impact spacecraft. Science, 326(5952), 565-568.**

- Takir, D., et al., 2013. Nature and degree of aqueous alteration in CM and CI carbonaceous chondrites. Meteorit. Planet. Sci. 48(9), 1618-1637.

- **Takir, D., Emery, J. P., 2012. Outer main belt asteroids: Identification and distribution of four 3-µm spectral groups. Icarus, 219(2), 641-654.**

- Takir, D., Emery, J.P., McSween, H.Y. Jr, 2015. Toward an understanding of phyllosilicate mineralogy in the outer main asteroid belt. Icarus 257, 185-193.

- Takir, D., Stockstill-Cahill, K.R., Hibbitts, C.A., Nakauchi, Y., 2019. 3-µm reflectance spectroscopy of carbonaceous chondrites under asteroid-like conditions. Icarus 333, 243–251.

- Tucker, O.J., Farrell, W.M., Killen, R.M., Hurley, D.M., 2019. Solar Wind Implantation Into the Lunar Regolith: Monte Carlo Simulations of H Retention in a Surface With Defects and the $H_2$ Exosphere. J. Geophys. Res. Planets 124, 278–293.

- **Usui, F., Hasegawa, S., Ootsubo, T., Onaka, T., 2019. AKARI/IRC near-infrared asteroid spectroscopic survey: AcuA-spec. Publ. Astron. Soc. Japan 71 (1), 1 (1–41), doi: 10.1093/pasj/psy125.**

- Walsh, K.J., Delbó, M., Bottke, W.F., Vokrouhlický, D., Lauretta, D.S., 2013. Introducing the Eulalia and new Polana asteroid families: Re-assessing primitive asteroid families in the inner Main Belt. Icarus 225(1), 283-297.

- Walsh, K.J., et al., 2019. Craters, boulders and regolith of (101955) Bennu indicative of an old and dynamic surface. Nat. Geosci. 12(4), 242-246.

- Zou, X.-D., et al., **2021.** Photometry of asteroid (101955) Bennu with OVIRS on OSIRIS-REx. Icarus **358, 114183, doi.org/10.1016/j.icarus.2020.114183.**

**Appendix A**: The selected meteorites are reported with their spectral reference and their H content calculated by Alexander et al., 2012, 2013 (*); Garenne et al., 2016 (**); Gilmore et al., 2019 (***). For each meteorite, the type and the subtype using the Rubin (2007) scale are reported, as well as the ones for which a Gaussian centered originally at 2.75µm was modelled ([1]).

| Name | H content | H error | Types | Subtypes | Spectrum Reference | H content Reference |
|---|---|---|---|---|---|---|
| ALH83100 | 1,353 | 0,009 | CM1/2 | 2.1 | Garenne et al., 2016 | * |
| ALH83100[1] | 1,353 | 0,009 | CM1/2 | 2.1 | Potin et al., 2020 | * |
| ALH84029 | 1,260 | 0,009 | CM1/2 | 2.1 | Garenne et al., 2016 | * |
| ALH84033 | 0,610 | 0,018 | CM2 Heated | / | Garenne et al., 2016 | * |
| ALH84044 | 1,240 | 0,008 | CM2 | 2.1 | Garenne et al., 2016 | * |
| Banten[1] | 0,910 | 0,010 | CM2 | 2.5 | Takir et al., 2019 | * |
| Cold Bokkeveld (*) [1] | 1,220 | 0,004 | CM2 | 2.2 | Takir et al., 2013 | * |
| DOM03183 | 0,950 | 0,001 | CM2 Heated | 2.3 | Garenne et al., 2016 | * |
| DOM08003[1] | 1,359 | 0,006 | CM2 | 2.2 | Potin et al., 2020 | * |
| EET83355 | 0,410 | 0,001 | CM2 Heated | / | Garenne et al., 2016 | * |
| EET96029 | 0,728 | 0,012 | CM2 Heated | / | Garenne et al., 2016 | * |
| EET96029[1] | 0,728 | 0,012 | CM2 Heated | / | Potin et al., 2020 | * |
| Essebi (*) [1] | 0,770 | 0,005 | CM2? | / | Takir et al., 2019 | * |
| Ivuna[1] | 1,330 | 0,094 | CI1 | / | Takir et al., 2013 | * |
| LAP02277[1] | 1,112 | 0,009 | CM1 Heated | 2.0 | Takir et al., 2013 | * |
| LAP02333 | 1,020 | 0,005 | CM2 | 2.6 | Garenne et al., 2016 | * |
| LAP02336 | 0,950 | 0,005 | CM2 | 2.6 | Garenne et al., 2016 | * |
| LEW87022 | 1,090 | 0,014 | CM2 | 2.3 | Garenne et al., 2016 | * |
| LEW90500 | 0,990 | 0,005 | CM2 | 2.3 | Garenne et al., 2016 | * |
| MAC88100[1] | 0,894 | 0,010 | CM2 Heated | 2.3 | Potin et al., 2020 | * |
| MET01070 | 1,274 | 0,000 | CM1 | 2.0 | Garenne et al., 2016 | * |
| MET01070[1] | 1,274 | 0,000 | CM1 | 2.0 | Potin et al., 2020 | * |
| Mighei (*) [1] | 0,994 | 0,003 | CM2 | 2.3 | Poggiali personal communicati | * |

| | | | | | | |
|---|---|---|---|---|---|---|
| | | | | | on | |
| MIL07700 | 0,570 | 0,016 | CM2 Heated | / | Garenne et al., 2016 | * |
| MIL07700[1] | 0,570 | 0,016 | CM2 Heated | / | Potin et al., 2020 | * |
| MIL07700[1] | 0,570 | 0,016 | CM2 Heated | / | Takir et al., 2013 | * |
| Murchison[1] | 0,956 | 0,002 | CM2 | 2.4 | Potin et al., 2020 | * |
| Murchison[1] | 0,956 | 0,002 | CM2 | 2.4 | Takir et al., 2019 | * |
| Orgueil BM[1] | 1,366 | 0,015 | CI1 | / | Potin et al., 2020 | * |
| Orgueil BM[1] | 1,366 | 0,015 | CI1 | / | Takir et al., 2019 | * |
| Orgueil Smith.[1] | 1,346 | 0,019 | CI1 | / | Potin et al., 2020 | * |
| Orgueil Smith.[1] | 1,346 | 0,019 | CI1 | / | Takir et al., 2019 | * |
| QUE97990[1] | 0,959 | 0,000 | CM2 | 2.5 | Potin et al., 2020 | * |
| QUE97990[1] | 0,959 | 0,000 | CM2 | 2.5 | Takir et al., 2013 | * |
| Tagish Lake lithology 4[1] | 0,642 | 0,000 | C2 | / | Potin et al., 2020 | *** |
| Tagish Lake[1] | 0,720 | 0,003 | C2 | / | Takir et al., 2019 | * |
| Tagish Lake[1] | 0,717 | 0,004 | C2 | / | Takir et al., 2019 | * |
| WIS91600 | 0,878 | 0,000 | CM2 Heated | / | Garenne et al., 2016 | ** |
| WIS91600[1] | 0,878 | 0,000 | CM2 Heated | / | Potin et al., 2020 | ** |

1022